HHS Public Access

Author manuscript

Magn Reson Med. Author manuscript; available in PMC 2018 September 01.

Published in final edited form as:

Magn Reson Med. 2017 September ; 78(3): 1070–1079. doi:10.1002/mrm.26506.

Accurate MR Thermometry by Hyperpolarized ^{129}Xe

Le Zhang[1,3], **Alex Burant**[2,3], **Andrew McCallister**[2,3], **Victor Zhao**[2], **Karl M. Koshlap**[4], **Simone Degan**[5], **Michael Antonacci**[2,3], and **Rosa Tamara Branca**[2,3,*]

[1]Department of Applied Physical Science, University of North Carolina at Chapel Hill, US

[2]Department of Physics and Astronomy, University of North Carolina at Chapel Hill, US

[3]Biomedical Research Imaging Center, University of North Carolina at Chapel Hill, US

[4]Eshelman School of Pharmacy, University of North Carolina at Chapel Hill, US

[5]Center for Molecular and Biomolecular Imaging, Department of Radiology and Dermatology, Duke University, Durham, NC

Abstract

Purpose—To investigate the temperature dependence of the resonance frequency of Lipid-Dissolved Xenon (LDX) and to assess the accuracy of LDX-based MR thermometry.

Methods—The chemical shift temperature dependence of water protons, methylene protons, and LDX was measured from samples containing tissues with varying fat contents using a high-resolution NMR spectrometer. LDX results were then used to acquire relative and absolute temperature maps in vivo and the results were compared to PRF-based MR thermometry.

Results—The temperature dependence of PRF is strongly affected by the specific distribution of water and fat. A redistribution of water and fat compartments can reduce the apparent temperature dependence of the water chemical shift from −0.01ppm/°C to −0.006ppm, whereas the LDX chemical shift shows a consistent temperature dependence of −0.21ppm/°C. The use of the methylene protons resonance frequency as internal reference improves the accuracy of LDX-based MR thermometry but degrades that of PRF-based MR thermometry as microscopic susceptibility gradients affected lipid and water spins differently.

Conclusion—The LDX resonance frequency, with its higher temperature dependence, provides more accurate and precise temperature measurements, both in vitro and in vivo. More importantly, the resonance frequency of nearby methylene protons can be used to extract absolute temperature information.

Keywords

MR thermometry; xenon; proton resonance frequency shift; adipose tissue

[*]Correspondence to: Rosa Tamara Branca, Ph.D.: Department of Physics and Astronomy, University of North Carolina at Chapel Hill, Chapel Hill, NC 27599, USA. rtbranca@unc.edu.

INTRODUCTION

In addition to providing real-time anatomical images to monitor the progress of treatments, MRI offers the possibility to measure temperature changes, non-invasively, in vivo in tissues. A variety of MR parameters are indeed sensitive to temperature. These include proton density (1), longitudinal (2,3) and transverse (4) relaxation times, water diffusion constant (5,6) and water proton resonance frequency (PRF) (7). Among them, PRF is the preferred temperature sensor as the water resonance frequency shifts linearly with temperature by about −0.01 ppm/°C over a wide temperature range and in different tissue types (8–10). One of the successful applications of PRF-based MR thermometry includes MR guided focused ultrasound (MRgFUS) of uterine fibroids (11), where MR thermometry is used to monitor, in real time, tissue temperature during thermal ablation by high intensity focused ultrasound (HIFU).

Traditionally, the phase difference between two images acquired pre- and post-heating is used to calculate the temperature change. However, in biological systems, any change in the local magnetic field caused by motion, field drift and macroscopic field inhomogeneities can easily overshadow the much smaller proton resonance frequency shift (PRFS) caused by temperature (12,13). Different approaches have been proposed to address this issue. These include model-based referenceless thermometry (14), multi-baseline correction methods (15,16), or both (17). Despite recent successful applications of these methods in MRgHIFU for the treatment of different types of cancer (18–20), tumors surrounded by fat tissues such as breast cancer still remain a challenge (21). In fatty tissues, inadvertent motion and phase-unwrapping errors caused by susceptibility gradients generated by water/fat interfaces can render temperature readings less accurate. The effect of such susceptibility gradients on the accuracy of MR thermometry was already analyzed previously by De Poorter et al (22) and, more recently, by Baron et al (23), who proposed a model-based correction method to estimate the proton resonance frequency shift caused by temperature-induced magnetic susceptibility changes in the presence of fat (24). Another way to improve the accuracy of PRF shift (PRFS) based MR thermometry is to use a ‘temperature independent’ resonance frequency, usually that of the methylene protons of nearby lipid molecules, as an internal reference to correct for field variations (25,26) or even to extract absolute temperature information (27). Unfortunately, since water and lipid spins always reside in different tissue or cell compartments, the effect of local susceptibility gradients cannot be completely removed, as also pointed out by Baron et al (23). To make matters worse, even though the resonance frequency of lipid spins remains virtually temperature independent over a wide range with a coefficient measured to be around +0.00018 ppm/°C (28), the magnetic susceptibility of fat has a relatively strong temperature dependence of 0.01 ppm/°C (22,29), which can lead to significant temperature-induced changes in the local magnetic field distribution, reducing the accuracy of PRF-based relative temperature measurements in the presence of fat.

Apart from ^{1}H, ^{129}Xe has attracted some interest as a potential temperature probe for MR thermometry. By virtue of having a large electron cloud, xenon’s chemical shift is very sensitive to changes in its physical and chemical environment. Schilling et al leveraged on this property to develop a ^{129}Xe-based temperature sensor (30). Specifically, the strong

chemical shift difference between cryptophane-bound (31) xenon and unbound xenon (−0.29 ppm/°C) was used to measure absolute temperature in vitro in an aqueous suspension containing the sensor at a concentration of 150 μM with an accuracy of 0.1° C.

More recently, our group showed that the chemical shift of xenon atoms naturally dissolved in adipose tissue, upon xenon inhalation, has a strong temperature dependence (32). The chemical shift temperature coefficient of lipid dissolved xenon (LDX), which we measured in vivo in mice, was found to be about −0.2 ppm/°C, similar to values previously reported for xenon dissolved in olive oil (−0.21 ppm/°C) and corn oil (−0.25 ppm/°C) (33). This strong temperature dependence, coupled with the high solubility of xenon in lipids, clearly opens up new opportunities for MR thermometry of fatty tissues in vivo. More interestingly, as LDX and methylene protons reside in the same tissue and cell compartment, lipid protons could be used as an internal temperature-insensitive reference to compensate for the effects of magnetic field drift, motion, and susceptibility gradients, at both macro and microscopic levels. To this end, in this paper we analyze the feasibility of LDX-based MR thermometry both in vitro and in vivo. Specifically, we first measured the temperature dependence of LDX, water protons and lipid protons in different in vitro adipose tissue samples. We then used this temperature dependence to assess the accuracy of LDX-based MR thermometry in vivo.

METHODS

Simulation

Water and fat spins always reside in different tissue and cell compartments and, as such, the effect of microscopic susceptibility gradients cannot be removed by referencing the water resonance frequency to that of nearby lipid protons.

To this end, simulations were carried out to evaluate the temperature-induced changes of the magnetic susceptibility gradients generated by different water-fat distributions and their effect on the resonance frequency of water and fat spins and on the accuracy of relative and absolute PRFS-based MR thermometry. Specifically, the local magnetic field perturbation due to magnetic susceptibility mismatch between water and fat compartments was first computed in MATLAB (MathWorks, Natick, MA), similarly to what was recently done by Baron et al (23). This was accomplished by using a Fourier based method first introduced by Deville et al (34) and by Salomir et al (35). Briefly, this approach takes advantage of the linear and local relation that exists in k-space between the z-component of the magnetization density, $M_z(\mathbf{k})$, and the z component of the magnetic field, $B_z(\mathbf{k})$:

$$B_z(\mathbf{k}) = M_z(\mathbf{k}) \cdot \frac{\mu_0}{3} \cdot (1 - 3\cos^2\beta), \quad (1)$$

where $\mu_0 = 1.2566\ T \cdot \mu m \cdot A^{-1}$ and β represents the angle between the vector **k** and the direction of the main magnetic field B_0. For each geometry, $M_z(\mathbf{k})$ is obtained by Fourier transforming the z-component of the magnetization density $M_z(\mathbf{r})$, calculated using the following relation:

$$M_z(\mathbf{r}) \approx \chi(\mathbf{r}) \frac{B_0}{\mu_0}, \quad (2)$$

which is valid since the magnetic susceptibility of water (−9.04 ppm (22)) and fat (−7.79 ppm (36)) are much smaller than 1. From $M_z(\mathbf{r})$, the resulting susceptibility field distribution $B_z(\mathbf{r})$ can then be obtained using Eqn. (1).

In our simulations, the computed $B_z(\mathbf{r})$ was superimposed onto the main magnetic field B_0 to calculate the evolution and apparent frequency shift of water and fat spins diffusing and dephasing in their respective compartments. Specifically, for each of the 4 different water-fat distributions analyzed (Figure 1), each consisting of a 128×128×128 matrix with an isotropic pixel size of 2.056 μm, we tracked the evolution of 25,000 spins for a total time of 2 s. During this time, each spin was allowed to evolve under the local magnetic field for a total time of 0.167 ms before diffusing to a different position. Diffusion was computed with a random walk Monte Carlo algorithm using a diffusion length L of 1.5 μm, calculated by using:

$$L = \sqrt{6 \cdot D \cdot \tau}, \quad (3)$$

with D being 2.22×10^{-3} $mm^2 \cdot s^{-1}$ (37) and $\boldsymbol{\tau}$=0.167 ms. A Fourier transform of the simulated FID was then performed to obtain a spectrum from which water and fat frequency shifts were determined.

In vitro high-resolution spectroscopic study

Muscle and white adipose tissue (WAT) were excised from the legs and abdominal regions of mice and rats right after euthanasia, while human WAT was harvested from the subcutaneous fat layer of a human cadaver. Tissues were not homogenized but minced and placed into O.D. 5 mm medium-walled NMR tubes to create 3 different samples, one containing human WAT (hWAT), one containing rodent WAT (rWAT) and one containing a mixture of rWAT and muscle. After introducing the sample into the NMR tube, the tube was connected to a vacuum/charge system equipped with a rotary pump, a precision pressure gauge (precision up to 0.01 psi) and a xenon cylinder. A long plastic hose, with a dead volume of about 317 cm^3, was used to connect the NMR tube to the vacuum/charge system, located outside of the 5 Gauss line of the fringe field of the spectrometer. Air from the entire system was first removed by the rotary vacuum pump, while the NMR tube was kept frozen in liquid nitrogen. After evacuating the entire system (NMR tube + connecting hose), ^{129}Xe (>86% isotopic enrichment) gas was introduced into the closed system until a specific pressure was reached. The NMR tube was then placed inside the magnet and remained connected through the hose to the vacuum/charge system for the entire duration of the experiment, to allow for monitoring and changing of ^{129}Xe pressure. The large dead volume of the system, in which O_2 was allowed to degas for at least 24 hours, guaranteed an in-tissue oxygen concentration of less than 10^{-5} amagat. ^{129}Xe pressure in the system was changed between 1 atm and 3 atm. After being charged and after each pressure change,

samples were allowed to stabilize for at least 24 hours. This time was chosen after measuring a sample's xenon-saturation time of about 18 hours by ^{129}Xe NMR spectroscopy.

All in vitro spectroscopic studies were made on a Varian Inova 500 MHz NMR Spectrometer (Varian NMR Systems, Palo Alto, California) using a ^{1}H-^{19}F/^{15}N-^{31}P PFG switchable broadband probe. First order and second order shim gradients were used to clearly resolve the water and CH_2 frequency line in the ^{1}H spectrum. A temperature controller (L900, Highland Technology, San Francisco, CA) was used to set and maintain sample temperature at a given value. Temperature values were calibrated with an accuracy of 0.1 °C at the beginning of each spectroscopy experiment by using the chemical shift separation between the methanol and methylene protons in a 100% methanol sample. All ^{1}H spectra were acquired using center frequency at 499.784378 MHz (arbitrarily defined as 0 ppm), repetition time (TR) of 3s, spectral width (SW) of 5997 Hz, 4096 points, 1 average and flip angle (FA) of 36° to minimize radiation damping effects. All ^{129}Xe spectra were acquired with center frequency at 138.268955 MHz (arbitrarily defined as 0 ppm), TR of 30s, SW of 29996 Hz, 14998 points, FA of 90°, and 64 – 128 averages, depending on spectral SNR.

In vivo imaging study

All in vivo animal studies were conducted under an animal protocol approved by the Institutional Animal Care and Use Committee at the University of North Carolina at Chapel Hill. For these studies, a total of 8 female obese (ob/ob) mice were used. Before the experiments, mice were first anesthetized with an IP injection of 75 mg/kg of pentobarbital (Nembutal, Abbott Laboratories). They were then intubated using a 22-gauge catheter (Sherwood Medical) and mechanically ventilated, using a hyperpolarized gas-compatible constant volume ventilator (38) at a rate of 100 breaths per minute. The gas mixture consisted of 75-vol% N_2 and 25-vol% O_2, for a total tidal volume of 0.2 ml. During ^{129}Xe imaging, 75-vol% N_2 was switched to 75-vol% of HP Xe.

To generate hyperpolarized ^{129}Xe, a gas mixture of 1% xenon (26.4% ^{129}Xe content), 10% N_2, and 89% He (Global Specialty Gases, Bethlehem, PA) was flowed through a Polarean 9800 ^{129}Xe Polarizer (Polarean, Inc., Durham, NC). A mass flow controller was used to regulate the flow rate of the gas mixture to 1.5 SLM, while the hyperpolarized xenon was cryogenically collected for a time of 15 minutes. The total gas pressure within the optical cell of the polarizer was maintained at 60 psi during collection. The temperature of the optical cell was controlled in two ways. First, forced air convection maintained the temperature of the oven, which housed the optical cell at 353 K. Second, heat tape was placed around the pre-saturation bulb of the optical cell and the temperature was kept at 453 K by an attached thermocouple. Upon the completion of gas collection, HP xenon was dispensed into a 350-mL Tedlar bag (Jensen Inert Products, Coral Springs, FL). The first sample of HP xenon for any study was placed inside a Polarean 2881 Polarization Measurement Station (Polarean Inc., Durham, NC) to determine the polarization level of xenon, with an average value of 10% across studies. Subsequent samples were immediately transferred to the ventilator.

Imaging experiments were performed on a 9.4T Bruker BioSpec 94/30 USR (Bruker BioSpin, Billerica, MA) spectrometer controlled by a console running ParaVision software. Mice were placed either supine (2 mice) or prone (6 mice) on a xenon surface coil (1-cm diameter, transmit and receive, resonant at 110.76 MHz, without ^{1}H decoupling) to select regions of the body with a different water/fat distribution. The surface coil was then positioned inside a ^{1}H volume coil (72-mm inner diameter, transmit and receive, resonant at 400 MHz).

^{1}H frequency maps were collected by using a chemical shift imaging (CSI) protocol that selected a 2 cm-thick axial slice centered on the ^{129}Xe surface coil. ^{129}Xe frequency maps were collected without slice selection, using an adiabatic BIR4 (B_1 insensitive rotation-4) pulse with a 90° flip angle. For both temperature maps we selected a Field of View (FOV) of 6 cm × 4 cm, a matrix size of 6×4 reconstructed to 16×16 or 32×32, 2048 points, an echo time (TE) of 20 ms for ^{129}Xe and 14 ms for ^{1}H, a TR of 12 s for ^{129}Xe and 4 s for ^{1}H. Anatomical ^{1}H images were also acquired using a gradient echo sequence (axial slice orientation, 20 mm thickness, 128×128 matrix, 6×6 cm FOV, TE=2.2 ms, TR=1 s) to provide anatomical reference.

For these experiments the body temperature of anesthetized mice, which are unable to control their body temperature under anesthesia, was allowed to equilibrate with bore temperature for at least 30 minutes before each measurement. Rectal temperature and bore temperature were measured and maintained within ±0.2 °C from the target temperature using a closed loop temperature control system (Small Animal Instruments, Inc., Stony Brook, NY). This included warm air circulating through the bore, a fiber optic temperature probe used to monitor bore temperature, and a fiber optic temperature probe used to monitor rectal temperature.

Data processing

Both in vitro and in vivo spectra were fit with custom MATLAB codes using a Voigt function to calculate the frequency of lipid-dissolved xenon. To calculate the absolute temperature, the chemical shift of LDX was referenced to the chemical shift of nearby methylene protons (rLDX) as follows. The methylene frequency was first placed at 1.3 ppm from a fictitious ^{1}H center frequency (fHCF). The LDX chemical shift was then calculated with respect to a fictitious ^{129}Xe center frequency (fXeCF), which is linked to the fHCF by: $\mathrm{fXeCF}=\mathrm{fHCF}\frac{\gamma_{Xe}}{\gamma_H}$. This way, the chemical shift difference between LDX and methylene protons (rLDX) could be easily calculated and compared for different samples and field strengths.

RESULTS

Figure 1 shows the local magnetic field disturbance produced by the susceptibility gradients for 4 different distributions of water and fat spins, while Table 1 shows the changes in the chemical shift of water and fat spins induced by the local susceptibility gradients. The magnetic susceptibility difference between water and fat compartments can change the water resonance frequency by as much as 0.2 ppm. More importantly, because water and fat spins

reside in different tissue compartments, their frequency is generally shifted in opposite directions and by different amounts and the resulting absolute temperature measurements can be off by several tens of degrees Celsius. In addition, because of the strong temperature dependence of the magnetic susceptibility of fat, when the relative temperature change is measured by using the chemical shift difference between water and fat spins, large temperature errors can also be made.

In Figure 2 we show representative ^{1}H and ^{129}Xe spectra acquired on the rWAT sample on the high-resolution NMR spectrometer and the temperature-induced shift on the water, methylene and lipid-dissolved xenon resonance frequencies. In the figure, a small shift toward higher frequencies (+0.0032 ppm/°C) can be observed in the methylene resonance frequency (Figure 2b), while water drifts toward lower frequencies with a larger temperature coefficient of −0.0089 ppm (2c). The LDX resonance frequency which, thanks to the high solubility of xenon in fat (39), was easily detected at relatively low gas pressures (~1 atm), also drifted towards lower frequency (2d) with a much higher temperature coefficient of −0.2 ppm/°C. Given the high SNR of both spectra and the relatively narrow line widths, we were able to determine xenon and methylene resonance frequencies with high accuracy in all samples. Specifically, the LDX resonance frequency was determined with an accuracy of better than 0.01ppm, except for the rWAT/Muscle sample. In this sample, the error in the determination of the LDX resonance frequency was slightly higher as the field inhomogeneity was not completely removed by shimming gradients. The water line width was also slightly higher (140 Hz) than in other samples, but still well resolved from the nearby methylene peaks (~1700 Hz downfield) such that we could determine the water resonance frequency with an accuracy of about 0.04 ppm. Interestingly, despite the presence of muscle in the rWAT/Muscle sample, due to the very low solubility of xenon in non-fatty tissues we were able to detect only the resonance frequency of LDX.

Figure 3 shows the temperature dependence of the water, methylene and LDX resonance frequency for rWAT, rWAT/Muscle and hWAT samples equilibrated at various xenon pressures. When temperature was increased, the methylene frequency (Fig 3a) slightly increased with a coefficient of about 0.003 ppm/°C in the rWAT and hWAT samples. In these samples, the water resonance frequency showed a temperature dependence similar to its nominal value of −0.01ppm/°C. As a result, when the water resonance frequency was referenced to the methylene resonance frequency (3c), the temperature coefficient of water increased for both samples (−0.011 ppm/°C in rWAT and −0.013 ppm/°C in hWAT). For the rWAT/muscle sample, on the other hand, the behavior was quite different. In this sample, the temperature dependence of the magnetic susceptibility of fat caused a variation of the local field distribution with temperature, which affected both water and methylene frequencies. Specifically, the methylene resonance frequency decreased instead of increasing with temperature, while the water resonance frequency showed much smaller temperature dependence, at least in the sample equilibrated at 1 atm (−0.0064 ppm/°C) (3b). In this sample, the distribution of water and fat spins drastically changed between the first set of measurements at 1atm and the second set of measurements at 3atm. It is noticeable that, in all samples, after the first set of measurements we observed a liquid phase floating on top of a more solid-like phase. Most likely, the breakdown of the adipocyte membranes led to the release of the lipid content of the cells. This separation did not affect the resonance

frequencies of the water and methylene spins in the two fat samples (hWAT and rWAT), but drastically affected that in the rWAT/Muscle sample. In this case, the redistribution of the two compartments pushed water and fat resonances in different directions, substantially changing the water-methylene resonance frequency difference by 0.37 ppm, and its temperature dependence from −0.0105 ppm/°C (measurement at 3 atm) to −0.0041 ppm/°C (measurement at 1 atm). As predicted by our simulations, as water and methylene protons reside in different tissue compartments, such redistribution led to a drastic change in the water-methylene resonance frequency difference.

The same figure also shows the temperature and pressure dependence of the LDX chemical shift in the same samples. By increasing xenon gas pressure in the system, an increasing amount of xenon dissolved in the sample, leading to an equivalent increase in LDX signal intensity (3d). As the figure 3(e) shows, the LDX resonance frequency presented a very similar temperature coefficient across all samples, averaging to −0.208 ppm/°C with a standard deviation of only 0.002 ppm/°C (3e). In addition, when the methylene spins were used as internal reference (3f), the difference in the chemical shift of the referenced LDX (rLDX) signal between the 3 samples decreased substantially, from 0.4 ppm to 0.3 ppm between the hWAT and rWAT sample, and from 0.2 ppm to less than 0.02 ppm between the rWAT and the rWAT/muscle sample. The larger difference in the rLDX frequency between the rWAT/Muscle and the hWAT sample suggests a small dependence of the LDX frequency on fat composition, which is expected to be different between the humans and rodents. An increase in rLDX frequency was also observed for pressure greater than 2.5atm. Specifically, at 3 atm the rLDX chemical shifts increased slightly by about 0.33 ppm. The chemical shift temperature dependence of LDX seemed to increase slightly as well between 2 atm and 3 atm, changing from −0.2089 ppm/°C to −0.2138 ppm/°C. We should point out that in all temperature studies we also noticed a small increase in xenon pressure as temperature was raised, most likely due to the temperature dependence of xenon solubility in fat. However, since this increase was smaller than 0.3 psi, it was not considered.

Interestingly, in the rWAT/muscle sample, despite the redistribution of water and fat compartments between the 1atm and 3 atm measurements, the rLDX was quite similar. Moreover, the temperature coefficient of rLDX was modified by less than 0.013 ppm/°C, while the temperature coefficient of the LDX-methylene chemical shift difference was modified even less by −0.011 ppm/°C. This result is not surprising. LDX and methylene spins reside in the same tissue compartment, thus they are always subjected to the same field perturbation. As such, the methylene spins represent a much better reference for LDX spins than they do for water protons, which reside in different tissue compartments and therefore are subjected to a different field perturbation. This clearly suggests that, by using the methylene spins as reference one always improves the accuracy of LDX-based thermometry, but not necessarily that of PRFS-based thermometry.

Figure 4 shows representative LDX relative temperature maps acquired in vivo from the abdomen of an anesthetized obese mouse acclimated at 3 different bore temperatures using the −0.21 ppm/°C LDX temperature coefficient found in vitro. All temperature maps display a temperature variation of less than 1 °C across the sensitive region of the coil. When two temperature maps were subtracted to calculate relative temperature changes, the apparent

temperature variation across the abdomen of the mouse dropped to less than 0.5 °C while the correct temperature change value was obtained within 0.3 °C.

Figure 5 shows water protons, methylene protons and LDX frequency maps for another mouse whose body temperature was equilibrated at two different temperatures, and the water and LDX temperature maps obtained by using the methylene frequency as an internal reference. The frequency maps of water and LDX spins across the mouse abdomen presented a similar variation of about 0.05 ppm for proton and 0.1 ppm for xenon. The methylene frequency variation in this case was much larger at about 0.35 ppm, mainly due to a poor methylene line shape. Because of these large variations in the methylene resonance frequency, the corrected PRF temperature maps presented a variation of about 40 °C, while the variation in the corrected LDX temperature maps decreased to less than 1 °C. The same figure also shows the corrected (referenced to the methylene resonance frequency) LDX resonance frequency as a function of rectal temperature as obtained from all in vivo studies, along with the values obtained from the rWAT and hWAT samples on the high-resolution spectrometer. Interestingly, the LDX-methylene values obtained in vivo match very well with those obtained in vitro from rWAT. In all 8 mice analyzed, the big uncertainty in the absolute chemical shift difference between methylene and LDX was rooted in the large uncertainty in the apparent methylene resonance frequency, which was caused by poor methylene line shapes across the mouse abdomen. This was the case whenever the mouse was placed supine on the xenon surface coil such that the sensitive region contained mainly a large water peak and a much weaker and distorted methylene peak.

DISCUSSION

One of the aims of this work was to measure the temperature coefficient of lipid-dissolved xenon in white adipose tissue under well-controlled pressure and temperature conditions. The temperature coefficient of LDX measured in this study was −0.208±0.002 ppm/°C, similar to what we previously found in vivo (32) and what has been reported in olive oil (33). Although the temperature dependence of LDX has never been investigated, we hypothesize that this dependence arises from the temperature-induced change in the density of the fat in which xenon dissolves. Because xenon has a large number of electrons, even a small change in the available volume between the triglyceride molecules in which it diffuses is expected to lead to a large change in its chemical shift.

We also showed that the use of methylene protons as an internal reference for the LDX chemical shift is able to completely remove the effect of macroscopic and microscopic magnetic field inhomogeneities. This is not surprising, as LDX and methylene protons reside in the same tissue compartment and experience the same field perturbation. Methylene protons, on the contrary, are not a good reference for water protons, as they reside in different compartments and experience different field perturbations. Consequently, variations in the water/fat spatial distribution are expected to lead to variations in the observed water-fat frequency difference (23) and, unless the exact distribution of water and fat spins is known at the sub-voxel level, PRF-based thermometry methods are expected to show an acceptable performance only at moderate temperature elevations and/or in voxels with low fat contents.

We also measured a small difference in chemical shift of less than 0.3 ppm between the LDX signal originating from hWAT and rWAT samples. This difference is more likely due to a different fatty acid profile between human adipose tissue and rodent adipose tissue, to which xenon is also expected to be sensitive.

A pressure dependence of the LDX frequency was also seen in samples equilibrated at pressures above 2.5 atm. This pressure dependence likely arose from Xe-Xe interactions, which were expected to have an impact only at very high concentrations of dissolved xenon. Considering the high solubility of xenon in adipose tissue, this pressure dependence seems to arise only for an in-tissue xenon concentration higher than 100 mM, i.e. orders of magnitude higher than the concentration achievable in vivo in tissues upon inhalation of the gas. As such, this pressure dependence is not expected to affect the accuracy of in vivo LDX MR thermometry.

Despite the high accuracy of LDX-based MR thermometry, a consideration must be made about its potential use in humans. With respect to previously proposed xenon-based temperature sensors, this method has the advantage that it does not require an in vivo injection of a contrast agent and can be performed after a single xenon inhalation. More importantly, it provides a direct measurement of tissue cell temperature. However, this method also requires the presence of lipids in which xenon should quickly dissolve before depolarizing at a concentration high enough for its detection. Since the achievable xenon concentration in tissue after a single inhalation of HP gas depends on blood flow, good targets for LDX-based MR thermometry would be the highly-perfused and lipid-rich brown adipose tissue (40), the brain and breast tumors. Tumors in the breast are generally highly vascularized and surrounded mostly by fat. More importantly, because of the presence of fat, in voxels on or near water-fat boundaries, temperature errors by PRF-based MR thermometry are known to be an issue (41). Brown adipose tissue is a fatty tissue that recently gained a lot of attention for its presumptive role in the regulation of body weight and glucose homeostasis (42). This tissue is specialized in heat production and, during stimulation of BAT thermogenesis, the increase in blood flow to this tissue leads to a specific uptake of xenon in BAT, both in mice (32) and in humans (43). Since the temperature of this tissue is expected to rise by 1–2 °C during thermogenesis, tracking of BAT temperature by LDX MR spectroscopy after a single inhalation of HP ^{129}Xe gas could be used to assess BAT thermogenic activity in humans, as has been done in mice (32). More recently, a LDX signal was also detected in the brain of human subjects inhaling 1 L of hyperpolarized xenon at 1.5 T (44). Although the LDX peak was attributed mainly to fat tissue outside the brain region, a strong signal originating from xenon dissolved in white matter was also detected. We speculate that this signal originates mostly from xenon dissolved in the myelin sheaths, which are composed mainly (~80 %) of lipids. Of course, temperature imaging based on LDX in humans would require large amounts of highly polarized HP ^{129}Xe gas, possibly coupled to multiple xenon inhalations, which may not be feasible given the known anesthetic effect of xenon at high concentrations. Nonetheless, although temperature monitoring may not be feasible at the temporal and spatial resolution required for hyperthermia treatments, we do foresee the use of LDX-based MR thermometry for temperature calibration at clinically relevant field strengths and for monitoring BAT thermogenesis in humans during

cold exposure. For other less-vascularized tissues, a better delivery of xenon to this tissue would be necessary.

CONCLUSION

In this work, the chemical shift temperature dependence of water protons, methylene protons, and lipid-dissolved xenon was measured in vitro for 3 different types of samples containing adipose tissue. Despite the strong similarity in composition between these samples, we observed a large variation in the chemical shift and in the temperature coefficient of the PRF, which means that, in the presence of fat, using the nominal −0.01 ppm/°C PRF temperature coefficient can be very unreliable for relative temperature measurements. Also, the magnitude of the water-fat chemical shift difference is strongly affected by the relative distribution of water and fat spins at the microscopic level and therefore it cannot be used for accurate absolute or relative temperature measurements. On the other hand, LDX and methylene spins reside in the same tissue compartment and, when the LDX is referenced to the methylene protons, both macro and microscopic magnetic field inhomogeneities can be completely removed, allowing more accurate and precise relative, as well as absolute, temperature measurements, both in vitro and in vivo.

Acknowledgments

This work was supported by National Institutes of Health grants DK056350 and DK108231.

References

1. Chen J, Daniel BL, Pauly KB. Investigation of proton density for measuring tissue temperature. Journal of Magnetic Resonance Imaging. 2006; 23(3):430–437. [PubMed: 16463298]
2. Graham SJ, Bronskill MJ, Henkelman RM. Time and temperature dependence of MR parameters during thermal coagulation of ex vivo rabbit muscle. Magnetic Resonance in Medicine. 1998; 39(2): 198–203. [PubMed: 9469702]
3. Hynynen K, McDannold N, Mulkern RV, Jolesz FA. Temperature monitoring in fat with MRI. Magnetic Resonance in Medicine. 2000; 43(6):901–904. [PubMed: 10861887]
4. Baron P, Ries M, Deckers R, Greef M, Tanttu J, Kohler M, Viergever MA, Moonen CTW, Bartels LW. In Vivo T-2-Based MR Thermometry in Adipose Tissue Layers for High-Intensity Focused Ultrasound Near-Field Monitoring. Magnetic Resonance in Medicine. 2014; 72(4):1057–1064. [PubMed: 24259459]
5. Lebihan D, Delannoy J, Levin RL. Temperature Mapping with Mr Imaging of Molecular-Diffusion - Application to Hyperthermia. Radiology. 1989; 171(3):853–857. [PubMed: 2717764]
6. Kozak LR, Bango M, Szabo M, Rudas G, Vidnyanszky Z, Nagy Z. Using diffusion MRI for measuring the temperature of cerebrospinal fluid within the lateral ventricles. Acta Paediatrica. 2010; 99(2):237–243. [PubMed: 19845565]
7. De Poorter J, De Wagter C, De Deene Y, Thomsen C, Stahlberg F, Achten E. Noninvasive MRI thermometry with the proton resonance frequency (PRF) method: in vivo results in human muscle. Magnetic Resonance in Medicine. 1995; 33(1):74–81. [PubMed: 7891538]
8. Hindman JC. Proton Resonance Shift of Water in Gas and Liquid States. Journal of Chemical Physics. 1966; 44(12):4582–92.
9. McDannold N. Quantitative MRI-based temperature mapping based on the proton resonant frequency shift: Review of validation studies. International Journal of Hyperthermia. 2005; 21(6): 533–546. [PubMed: 16147438]

10. Peters RD, Hinks RS, Henkelman RM. Ex vivo tissue-type independence in proton-resonance frequency shift MR thermometry. Magnetic Resonance in Medicine. 1998; 40(3):454–459. [PubMed: 9727949]
11. Kim YS, Trillaud H, Rhim H, Lim HK, Mali W, Voogt M, Barkhausen J, Eckey T, Kohler MO, Keserci B, et al. MR thermometry analysis of sonication accuracy and safety margin of volumetric MR imaging-guided high-intensity focused ultrasound ablation of symptomatic uterine fibroids. Radiology. 2012; 265(2):627–637. [PubMed: 23012465]
12. Bolan PJ, Henry PG, Baker EH, Meisamy S, Garwood M. Measurement and correction of respiration-induced B-0 variations in breast H-1 MRS at 4 tesla. Magnetic Resonance in Medicine. 2004; 52(6):1239–1245. [PubMed: 15562472]
13. Young IR, Hajnal JV, Roberts IG, Ling JXX, HillCottingham RJ, Oatridge H, Wilson JA. An evaluation of the effects of susceptibility changes on the water chemical shift method of temperature measurement in human peripheral muscle. Magnetic Resonance in Medicine. 1996; 36(3):366–374. [PubMed: 8875406]
14. Rieke V, Vigen KK, Sommer G, Daniel BL, Pauly JM, Butts K. Referenceless PRF shift thermometry. Magnetic Resonance in Medicine. 2004; 51(6):1223–1231. [PubMed: 15170843]
15. de Senneville BD, Mougenot C, Moonen CTW. Real-time adaptive methods for treatment of mobile organs by MRI-controlled high-intensity focused ultrasound. Magnetic Resonance in Medicine. 2007; 57(2):319–330. [PubMed: 17260361]
16. Vigen KK, Daniel BL, Pauly JM, Butts K. Triggered, navigated, multi-baseline method for proton resonance frequency temperature mapping with respiratory motion. Magnetic Resonance in Medicine. 2003; 50(5):1003–1010. [PubMed: 14587011]
17. Grissom WA, Rieke V, Holbrook AB, Medan Y, Lustig M, Santos J, McConnell MV, Pauly KB. Hybrid referenceless and multibaseline subtraction MR thermometry for monitoring thermal therapies in moving organs. Medical Physics. 2010; 37(9):5014. [PubMed: 20964221]
18. McDannold N, Tempany C, Jolesz F, Hynynen K. Evaluation of referenceless thermometry in MRI-guided focused ultrasound surgery of uterine fibroids. Journal of Magnetic Resonance Imaging. 2008; 28(4):1026–1032. [PubMed: 18821603]
19. Holbrook AB, Santos JM, Kaye E, Rieke V, Pauly KB. Real-time MR thermometry for monitoring HIFU ablations of the liver. Magnetic Resonance in Medicine. 2010; 63(2):365–373. [PubMed: 19950255]
20. Pichardo S, Köhler M, Lee J, Hynnyen K. In vivo optimisation study for multibaseline MR-based thermometry in the context of hyperthermia using MR-guided high intensity focused ultrasound for head and neck applications. International Journal of Hyperthermia. 2014; 30(8):579–592. [PubMed: 25430989]
21. Merckel LG, Bartels LW, Köhler MO, van den Bongard HJGD, Deckers R, Mali WPTM, Binkert CA, Moonen CT, Gilhuijs KGA, van den Bosch MAAJ. MR-Guided High-Intensity Focused Ultrasound Ablation of Breast Cancer with a Dedicated Breast Platform. CardioVascular and Interventional Radiology. 2013; 36(2):292–301. [PubMed: 23232856]
22. De Poorter J. Noninvasive MRI thermometry with the proton resonance frequency method: Study of susceptibility effects. Magnetic Resonance in Medicine. 1995; 34(3):359–367. [PubMed: 7500875]
23. Baron P, Deckers R, Bouwman JG, Bakker CJG, de Greef M, Viergever MA, Moonen CTW, Bartels LW. Influence of water and fat heterogeneity on fat-referenced MR thermometry. Magnetic Resonance in Medicine. 2016; 75(3):1187–1197. [PubMed: 25940426]
24. Baron P, Deckers R, de Greef M, Merckel LG, Bakker CJG, Bouwman JG, Bleys RLAW, van den Bosch MAAJ, Bartels LW. Correction of proton resonance frequency shift MR-thermometry errors caused by heat-induced magnetic susceptibility changes during high intensity focused ultrasound ablations in tissues containing fat. Magnetic Resonance in Medicine. 2014; 72(6):1580–1589. [PubMed: 24347129]
25. Soher BJ, Wyatt C, Reeder SB, MacFall JR. Noninvasive temperature mapping with MRI using chemical shift water-fat separation. Magnetic Resonance in Medicine. 2010; 63(5):1238–1246. [PubMed: 20432295]

26. Shmatukha AV, Harvey PR, Bakker CJG. Correction of proton resonance frequency shift temperature maps for magnetic field disturbances using fat signal. Journal of Magnetic Resonance Imaging. 2007; 25(3):579–587. [PubMed: 17335067]
27. Sprinkhuizen SM, Bakker CJG, Bartels LW. Absolute MR thermometry using time-domain analysis of multi-gradient-echo magnitude images. Magnetic Resonance in Medicine. 2010; 64(1): 239–248. [PubMed: 20577981]
28. Stollberger R, Ascher PW, Huber D, Renhart W, Radner H, Ebner F. Invited. Temperature monitoring of interstitial thermal tissue coagulation using MR phase images. Journal of Magnetic Resonance Imaging. 1998; 8(1):188–196. [PubMed: 9500279]
29. Sprinkhuizen SM, Bakker CJG, Ippel JH, Boelens R, Viergever MA, Bartels LW. Temperature dependence of the magnetic volume susceptibility of human breast fat tissue: an NMR study. Magnetic Resonance Materials in Physics, Biology and Medicine. 2012; 25(1):33–39.
30. Schilling F, Schroder L, Palaniappan KK, Zapf S, Wemmer DE, Pines A. MRI Thermometry Based on Encapsulated Hyperpolarized Xenon. Chemphyschem. 2010; 11(16):3529–3533. [PubMed: 20821795]
31. Sears DN, Jameson CJ. Theoretical calculations of the Xe chemical shifts in cryptophane cages. Journal of Chemical Physics. 2003; 119(23):12231–12244.
32. Branca RT, He T, Zhang L, Floyd CS, Freeman M, White C, Burant A. Detection of brown adipose tissue and thermogenic activity in mice by hyperpolarized xenon MRI. Proceedings of the National Academy of Sciences. 2014; 111(50):18001–18006.
33. Venkatesh, A., Kacher, DK., Kuroda, K., Balamore, D., Jolesz, F., Albert, M. Temperature measurement using the 129Xe chemical shift. Proceedings of the International Society of Magnetic Resonance in Medicine; Glasgow, Scotland, UK. 2001.
34. Deville G, Bernier M, Delrieux JM. NMR multiple echoes observed in solid He3. Physical Review B. 1979; 19(11):5666–5688.
35. Salomir R, de Senneville BD, Moonen CT. A fast calculation method for magnetic field inhomogeneity due to an arbitrary distribution of bulk susceptibility. Concepts in Magnetic Resonance. 2003; 19B(1):26–34.
36. Hopkins JA, Wehrli FW. Magnetic susceptibility measurement of insoluble solids by NMR: Magnetic susceptibility of bone. Magnetic Resonance in Medicine. 1997; 37(4):494–500. [PubMed: 9094070]
37. Jones JR, Rowlands DL, Monk CB. Diffusion Coefficient of Water in Water and in Some Alkaline Earth Chloride Solutions at 25°C. Transactions of the Faraday Society. 1965; 61:1384–1388.
38. Nouls J, Fanarjian M, Hedlund L, Driehuys B. A constant-volume ventilator and gas recapture system for hyperpolarized gas MRI of mouse and rat lungs. Concepts in Magnetic Resonance Part B: Magnetic Resonance Engineering. 2011; 39B(2):78–88. [PubMed: 21625347]
39. Steward A, Allott PR, Cowles AL, Mapleson WW. Solubility coefficients for inhaled anaesthetics for water, oil and biological media. British Journal of Anaesthesia. 1973; 45(3):282–93. [PubMed: 4573000]
40. Cannon B, Nedergaard J. Brown Adipose Tissue: Function and Physiological Significance. Physiological Reviews. 2004; 84(1):277–359. [PubMed: 14715917]
41. Sprinkhuizen SM, Konings MK, van der Bom MJ, Viergever MA, Bakker CJG, Bartels LW. Temperature-induced tissue susceptibility changes lead to significant temperature errors in PRFS-based MR thermometry during thermal interventions. Magnetic Resonance in Medicine. 2010; 64(5):1360–1372. [PubMed: 20648685]
42. Lidell ME, Betz MJ, Enerbäck S. Brown adipose tissue and its therapeutic potential. Journal of Internal Medicine. 2014; 276(4):364–377. [PubMed: 24717051]
43. Branca, RT., Zhang, L., Burant, A., Katz, L., McCallister, A. International Society of Magnetic Resonance in Medicine. Singapore: 2016. Detection of human brown adipose tissue by MRI with hyperpolarized Xe-129 gas and validation by FDG-PET/MRI; p. 1054
44. Rao M, Stewart NJ, Norquay G, Griffiths PD, Wild JM. High resolution spectroscopy and chemical shift imaging of hyperpolarized 129 Xe dissolved in the human brain in vivo at 1.5 tesla. Magnetic Resonance in Medicine. 2016; 75(6):2227–2234. [PubMed: 27080441]

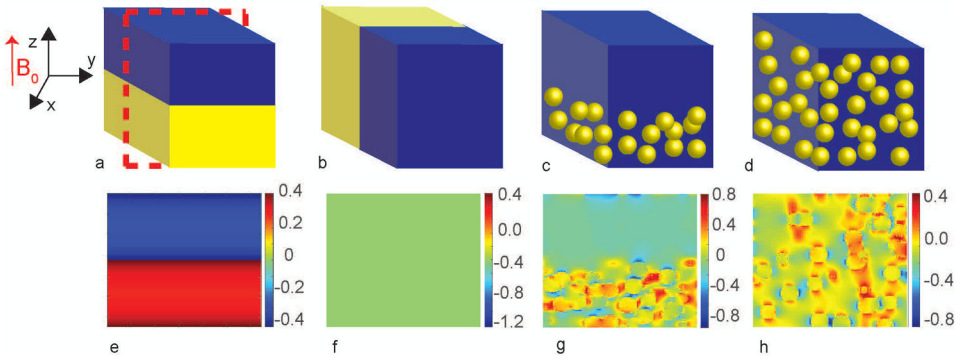

Figure 1.

Water-fat distribution geometries simulated in this study (a, b, c and d) and their associated magnetic field perturbation (e, f, g and h) produced by the magnetic susceptibility mismatch between water and fat compartments. In figures a–d, the yellow color represents the fat compartment while the blue color represents the water compartment. For each geometry, field maps are reported for the center YZ slice (dotted square in a). (2-columns)

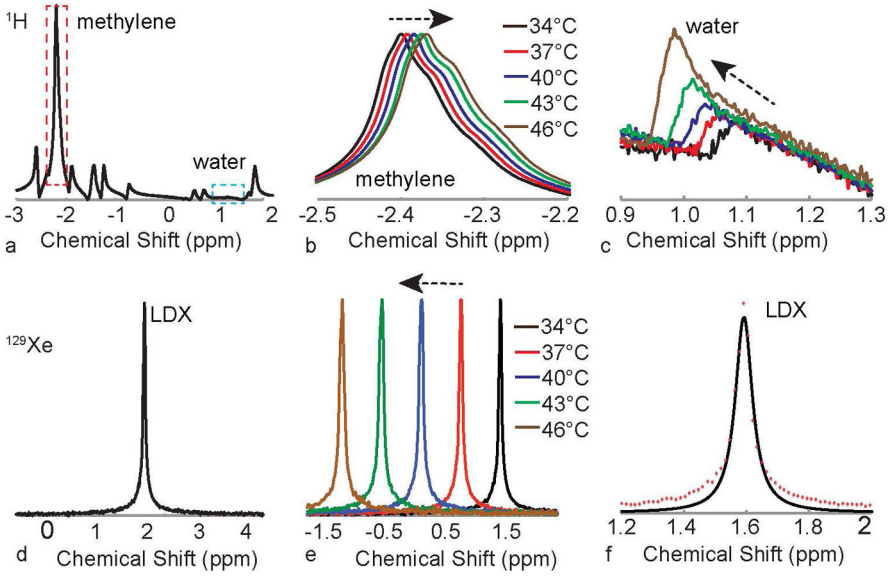

Figure 2.

^{1}H and ^{129}Xe spectra acquired on rWAT sample equilibrated at 3atm. (a) ^{1}H spectrum at 34°C. Water and methylene peaks are highlighted by the blue and red dashed boxes, respectively. The ^{1}H center frequency was arbitrarily set at 0 ppm, leaving the methylene spins at around −3.1 ppm and the water spins at around 0.4 ppm at 26°C. (b) Shift of the methylene resonance frequency line with temperature. (c) Shift of the water resonance frequency line with temperature. (d) ^{129}Xe spectrum at 26°C showing a single peak: the Lipid Dissolved Xenon (LDX) peak. (e) Shift of LDX peak with temperature. (f) MATLAB fit of the LDX resonance at 26°C. (1.5-columns)

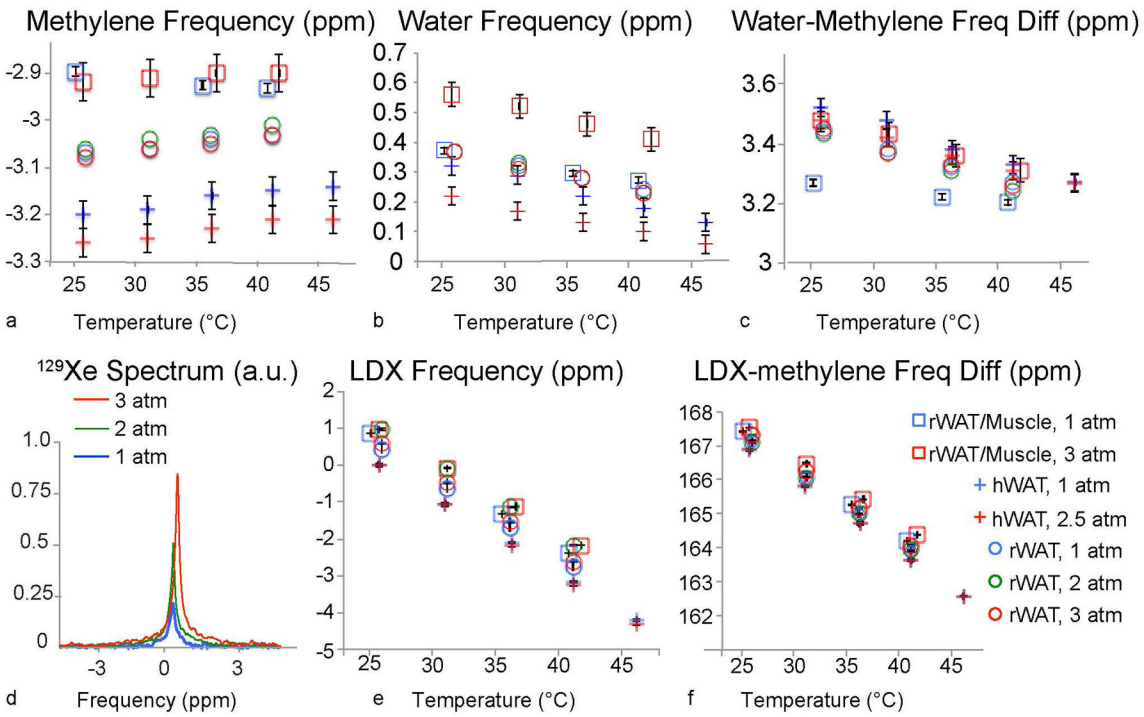

Figure 3.

Temperature dependence of water, methylene, and lipid-dissolved xenon resonance frequencies for three different adipose tissue samples equilibrated at different xenon gas pressures. (a) Temperature dependence of the methylene resonance frequency. (b) Temperature dependence of the water resonance frequency. (c) Temperature dependence of the water-methylene resonance frequency difference. (d) ^{129}Xe spectra at 26 °C for the rWAT sample at different xenon gas pressures. (e) Temperature dependence of the lipid-dissolved xenon resonance frequency. (f) Temperature dependence of the lipid-dissolved xenon-methylene resonance frequency difference. (2-columns)

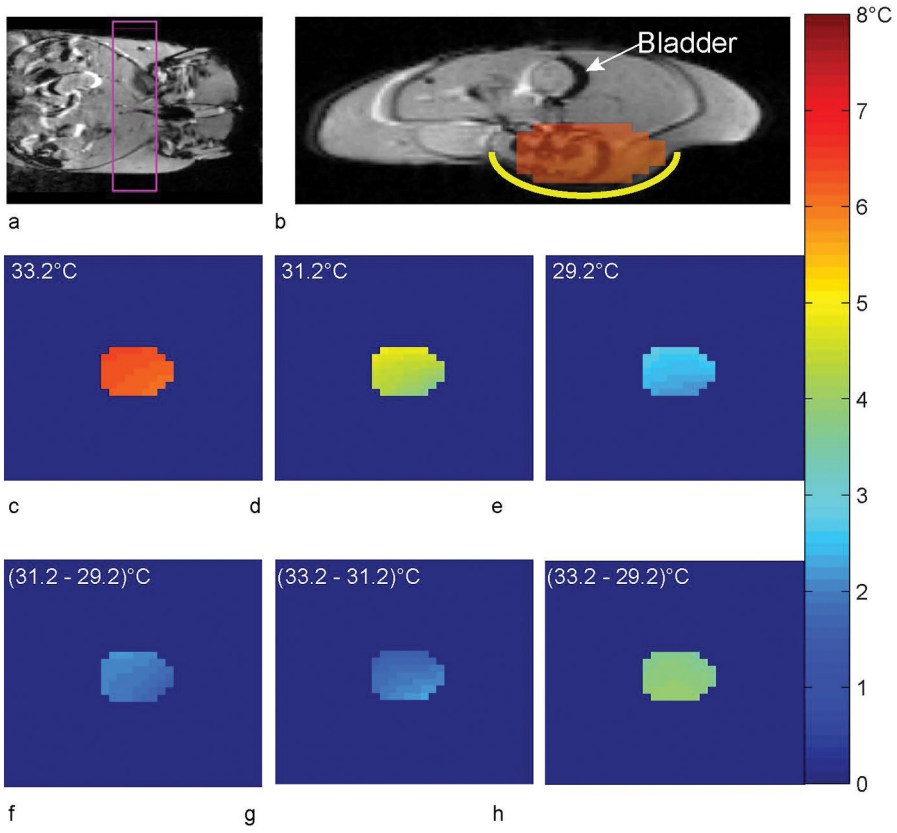

Figure 4.

In vivo temperature maps obtained from an obese mouse using the LDX frequency as temperature sensor. (a) Coronal view showing the selected axial slice. The mouse was positioned supine and the position of the Xe surface coil is indicated by the yellow line. (b) LDX temperature map overlaid on the axial ^{1}H reference image. (c)–(e) LDX temperature maps acquired with the mouse body temperature equilibrated at 3 different temperatures. A coefficient of −0.21 ppm/°C was used for all temperature maps (f–h) Relative temperature change maps showing the correct average temperature change (2°C for f and g, and 4 °C for h). (1.5-columns)

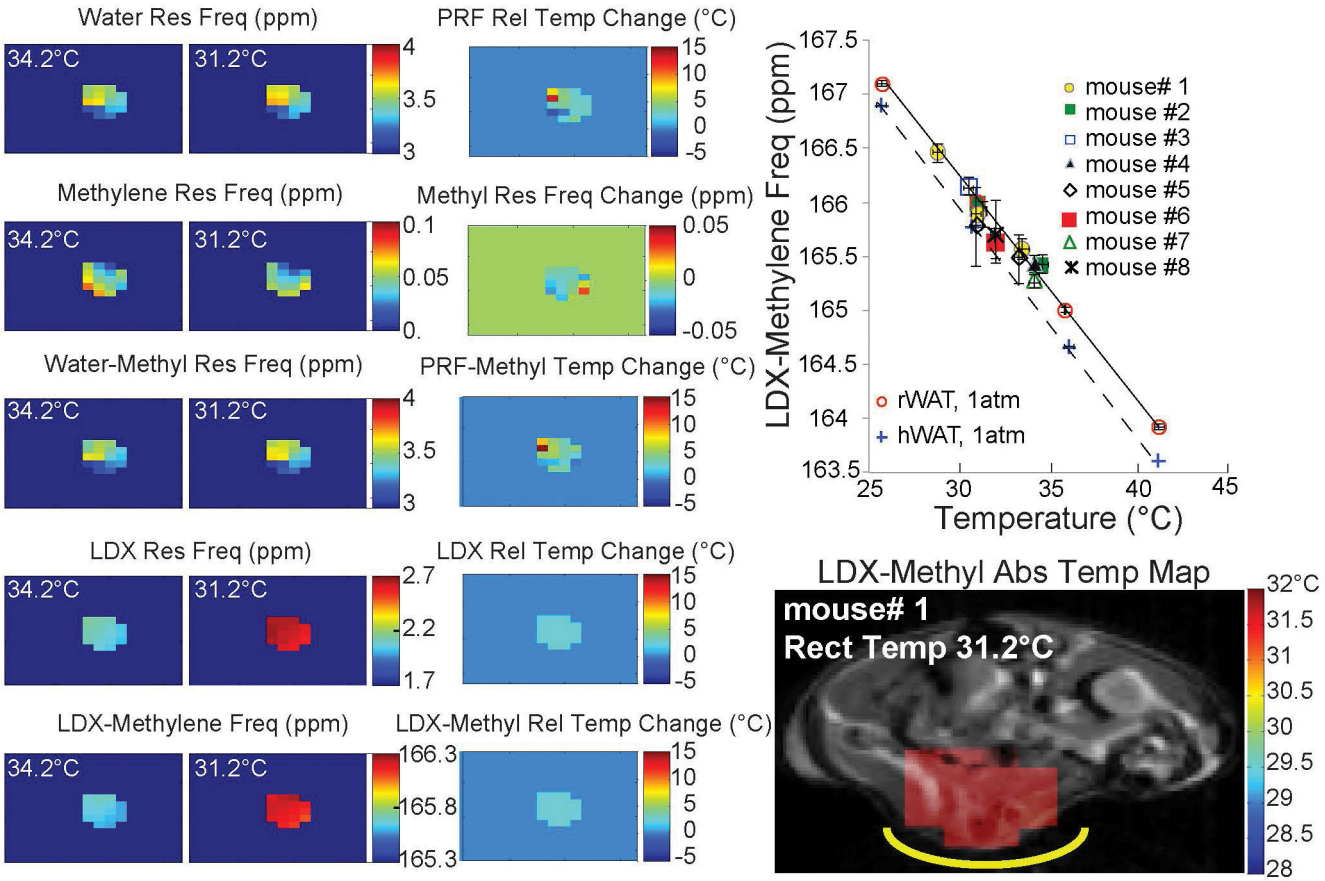

Figure 5.

Frequency and temperature maps acquired in vivo from an obese mouse whose body temperature was equilibrated at two different temperatures: 31.2°C and 34.2°C. (a) Water, methylene, water-methylene, LDX and LDX-methylene resonance frequencies. (b) Temperature maps showing the relative temperature change between the two measurements obtained by using a temperature coefficient of −0.01ppm/°C for both the water resonance frequency and the water-methylene resonance frequency difference, and a temperature coefficient of −0.21 ppm/°C for the LDX resonance frequency and LDX-methylene resonance frequency difference. (c) LDX-methylene resonance frequency obtained in vitro for the rWAT sample overlapped with that obtained in vivo showing the difference in LDX frequencies. (d) Absolute temperature map obtained at 31.2°C using the LDX-methylene resonance frequency difference. The mouse was positioned supine and the coil position is indicated by the yellow line. The real temperature is overestimated by less than 0.5°C. (2-columns)

Table 1

Computed resonance frequency shifts of water and methylene protons caused by magnetic susceptibility gradients for different water-fat distributions at two different temperatures. The table also shows the temperature error made when the water-methylene resonance frequency difference is used to calculate absolute temperature and when it is used to calculate relative temperature changes.

Geometry	**A**		**B**		**C**		**D**	
Temperature (°C)	0	5	0	5	0	5	0	5
$\Delta\omega_{water}$ (ppm)	−0.04	−0.04	0.082	0.089	0.209	0.216	0.125	0.127
$\Delta\omega_{fat}$ (ppm)	0.063	0.066	0.016	0.012	0.082	0.085	0.056	−0.058
$\Delta\omega_{water}-\Delta\omega_{fat}$	−0.103	−0.106	0.066	0.077	0.127	0.131	0.069	0.185
Absolute temperature error using $\omega_{water}-\omega_{fat}$ (°C)	10.3	10.6	−6.6	−7.7	12.7	13.1	−6.9	−18.5
Relative temperature error using $\Delta(\omega_{water}-\omega_{fat})$ (°C)	4.7		5.3		4		5.4	
Relative temperature error using ω_{water} (°C)	0		4.3		4.3		4.8	